# Miniaturized fiber-coupled confocal fluorescence microscope with an electrowetting variable focus lens using no moving parts

**Baris N. Ozbay,[1] Justin T. Losacco,[2] Robert Cormack,[3] Richard Weir,[1] Victor M. Bright,[4] Juliet T. Gopinath,[3] Diego Restrepo,[2] and Emily A. Gibson[1,*]**

[1]*Department of Bioengineering, University of Colorado Anschutz Medical Campus, Aurora, Colorado 80045, USA*

[2]*Department of Cell and Developmental Biology, University of Colorado Anschutz Medical Campus, Aurora, Colorado 80045, USA*

[3]*Department of Electrical, Computer and Energy Engineering, University of Colorado Boulder, Colorado 80309, USA*

[4]*Department of Mechanical Engineering, University of Colorado Boulder, Colorado 80309, USA*

**Corresponding author: Emily.Gibson@ucdenver.edu*

Received March 24, 2015; revised April 27, 2015; accepted April 29, 2015;
posted April 30, 2015 (Doc. ID 236814); published May 22, 2015

We report a miniature, lightweight fiber-coupled confocal fluorescence microscope that incorporates an electrowetting variable focus lens to provide axial scanning for full three-dimensional (3D) imaging. Lateral scanning is accomplished by coupling our device to a laser-scanning confocal microscope through a coherent imaging fiber-bundle. The optical components of the device are combined in a custom 3D-printed adapter with an assembled weight of <2 g that can be mounted onto the head of a mouse. Confocal sectioning provides an axial resolution of ~12 μm and an axial scan range of ~80 μm. The lateral field-of-view is 300 μm, and the lateral resolution is 1.8 μm. We determined these parameters by imaging fixed sections of mouse neuronal tissue labeled with green fluorescent protein (GFP) and fluorescent bead samples in agarose gel. To demonstrate viability for imaging intact tissue, we resolved multiple optical sections of *ex vivo* mouse olfactory nerve fibers expressing yellow fluorescent protein (YFP). 

*OCIS codes:* (110.2350) Fiber optics imaging; (170.2150) Endoscopic imaging; (170.2520) Fluorescence microscopy; (220.3620) Lens system design; (170.0110) Imaging systems; (170.3880) Medical and biological imaging.
http://dx.doi.org/10.1364/OL.40.002553

Laser-scanning microscopy (LSM), using confocal or multiphoton methods, is a powerful technique for *in vivo* physiological imaging [1–4]. The primary advantage of LSM is the ability to extract thin optical sections, important for imaging cells in thick tissue. Optical sectioning combined with axial scanning enables the collection of three-dimensional (3D) data from tissue. This technique is especially useful for functional imaging of cellular network dynamics, which often appear in multiple focal planes [3]. In order to apply these methods for 3D imaging in freely moving mice, a lightweight and compact fiber-coupled microscope (FCM) must be designed with high-speed axial focusing capability.

Here we demonstrate a laser-scanning FCM for confocal fluorescence imaging, using a high-speed variable focus electrowetting lens (EL) for axial scanning requiring no mechanically moving parts. This design allows stable 3D fluorescence imaging of tissue. The implantable portion of the device is 1 mm in diameter, and the entire FCM including electrowetting lens weighs <2 g and can achieve an imaging volume of ~300 μm diameter × 80 μm depth with sub-cellular resolution. These design parameters are important for a head-mounted device for potential imaging of the brain in freely moving mice. In addition, we present confocal imaging of YFP- and GFP-labeled brain tissue.

Previous work has demonstrated FCMs using a single optical fiber coupled with distal miniature two-dimensional (2D) scanners (for review see [5–7]) or by scanning proximally through a high-density coherent fiber bundle [8–10]. Although such devices demonstrate axial sectioning, imaging is typically performed at a fixed focal depth. Multi-focal techniques have been demonstrated in FCM systems. Examples include micromotors [11], piezoelectric actuators [12], thermomechanical actuators [13], micro-electromechanical systems (MEMS) mirrors [14,15], and variable focus lenses [16]. However, mechanical actuators have low bandwidth and can introduce movement artifacts. Micro-mirrors have relatively low reflectivity and require complex optical setups. Other designs that image multiple fixed focal planes have been demonstrated [17,18], but do not allow for continuous focusing.

Variable focus lenses have been shown to allow axial scanning with no mechanical actuation for various microscopy applications [19–22]. Variable focus lenses for endoscopes have also been demonstrated, including a shape-changing polymer lens [20] and a pressure-driven liquid lens [16]. However, these lenses are too slow or sensitive to orientation and motion for imaging on an awake animal. Electrowetting lenses (EL) allow for variable focus by using an applied electric field to change the curvature between two immiscible fluids [23]. They have several advantages for *in vivo* 3D imaging, including a high scan speed (~50 Hz over the full focal range), long-term repeatability, and ability to operate in any orientation since their operation is dominated by surface tension, not gravity [24,25].

In Fig. 1(a), we show the imaging setup incorporating a commercial EL in the focusing optics. A laser-scanning confocal microscope (Leica SP5 II) provides the continuous wave laser for fluorescence excitation, steering of the beam laterally using a resonance beam scanner, and spectrally filtered detectors. To fiber-couple our device to the microscope, we use a high-density coherent fiber-bundle with 0.5-m length, 30,000 count fiber cores,

 

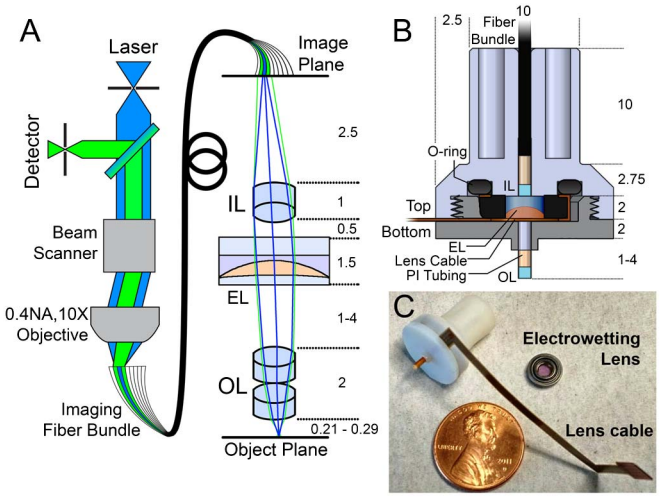


Fig. 1. Imaging system (dimensions in mm). (a) Laser scanning confocal microscope coupled to distal imaging optics through fiber bundle (IL, imaging lens; EL, electrowetting lens; OL, objective lenses). (b) CAD model of adapter with optics. Blue, top section. Gray, bottom section. (c) Photo of assembled adapter and EL.

total effective imaging diameter of 0.8 mm, 2.5-μm core diameter, and 4.5-μm inter-core spacing (Fujikura, FIGH-30-850N). The excitation laser is focused onto the proximal surface of the fiber-bundle by a 10× 0.4 numerical aperture (NA) objective. Imaging over a single focal plane is performed by raster-scanning the laser into individual fiber cores. The light from the fiber is collimated with a 3-mm focal length achromatic lens (Edmund Optics, 65-566), passes through the EL, and is focused onto our sample using two 2-mm focal length achromatic lenses (Edmund Optics, 65-565). The imaging system has ∼2.5× magnification. For each fiber core, fluorescence emission is transmitted back through the optics into the same fiber core and registered on the confocal microscope internal photomultiplier detector. The EL is placed in the infinity space of the telescopic imaging system, where changing the focal length of the EL by voltage results in a shift of the front focal length of the FCM. We used a commercial tunable lens (Arctic 316, Varioptic Inc.), which has an effective focal length that ranges from −57 to +29 mm (−17 to 36 $m^{-1}$ in diopters) corresponding to a voltage input from 25 to 60 $V_{RMS}$ provided through a flexible cable. Typical power draw of the EL is ∼15 mW. We designed a custom-fabricated two-part plastic adapter [shown in cross section in Fig. 1(b)] to provide a lightweight and rigid enclosure for the imaging optics, including the 7.75-mm diameter EL package. The adapter is designed to be surgically attached on a mouse head with the 1-mm diameter objective lens inserted for deep brain imaging. The top section is easily detachable, and the bottom section is designed with a low profile (<5 mm height) such that it may remain implanted for long-term imaging. The EL and electrode are clamped between the two adapter sections and held in place with an O-ring. In this design, the EL is positioned away from the tissue to be imaged by ∼2 mm, which provides adequate insulation from the electrical contact. The objective lenses are glued with cyanoacrylate adhesive into a length (3–7 mm) of polyimide tubing with 1.06-mm outer diameter and fit into the bottom of the holder. Figure 1(c) shows a photograph of the assembled FCM after being manufactured via a 0.1–0.2-mm tolerance 3D-printing process. The parts are precise enough to maintain accurate optical alignment over repeated assemblies. The final assembly weighs approximately 1.9 g, comparable in size and weight to current miniature head-mounted microscopes for awake-behaving imaging [26].

We used Zemax optical design software to compute the optical performance of our FCM with the objective lens extending 1 mm below the adapter, for surface level imaging, and 4 mm below the adapter, for deep tissue imaging. The adjustable design permits access to different regions of interest in the brain. We obtained model files for the lenses from Edmund Optics and Varioptic. Due to the selection of achromatic lenses, and we see minimal chromatic aberrations for wavelengths ∼500–600 nm. Results from the design are summarized in Table 1. The range in parameters are over the full focus range of the EL.

The lateral resolution is determined by the fiber-bundle core-spacing (4.5 μm) demagnified by the optics, verified experimentally in Fig. 4. The optics are required to have good performance only up to the maximum spatial frequency resolvable by the fiber-bundle, which is 300 line pairs (lp)/mm. We calculate the effective field-of-view (FOV) by finding the minimum object field diameter at which the modulation of the optical transfer function (MTF) at 300 lp/mm fails to meet the Rayleigh criterion (MTF > 0.2) [27]. The model shows a constant field curvature that results in a ∼20 μm axial focus shift at the edge of the FOV compared to the center, which is managed by imaging thick tissue (>20 μm) or by combining multiple optical sections. As the objective lens position is increased further from the adapter, there is an increase in off-axis vignetting and aberrations, most significantly astigmatism and distortion. Therefore, the FOV at the 4-mm objective position is predicted to be smaller due to the increased aberrations and vignetting.

We evaluated the FOV experimentally by imaging a 15-μm-thick section of mouse brain showing neuroglial oligodendrocyte cells expressing GFP. Figure 2(a) shows a standard confocal fluorescence image of the sample using 488-nm excitation light. We compensated for the field curvature by performing a maximum intensity projection of 3–4 axial planes, obtained by varying the EL focus. Figures 2(b) and 2(c) show images for the 1- and 4-mm objective lens positions. At the 4-mm position, there is a reduction in FOV due to off-axis vignetting and

**Table 1. FCM Optical Parameters**

| Objective Position (mm) | Scan Range (μm) | Magnification | Lateral Resolution (μm) | Field-of-view (μm) | NA |
|---|---|---|---|---|---|
| 1 | 211–288 | 2.4–2.6 | 1.8–1.7 | ∼300 | 0.36–0.35 |
| 4 | 212–290 | 2.2–2.7 | 2.0–1.7 | ∼240 | 0.41–0.35 |

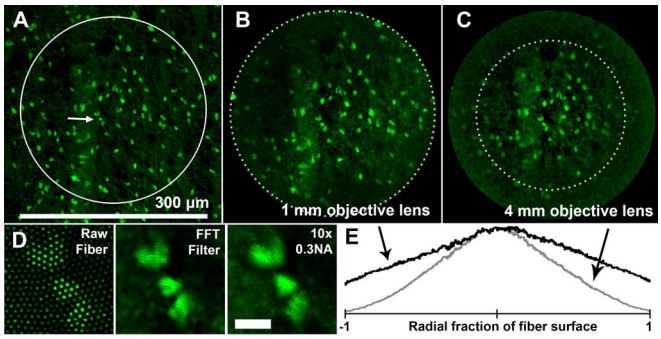


Fig. 2. Lateral imaging characteristics of FCM at different objective depths. (a) GFP-labeled neuroglia imaged with 20X, 0.8 NA objective. (b) Same region imaged with FCM at shortest and (c) longest objective position. (d) Zoom-in showing the cell bodies indicated by white arrow. Left: FCM image showing pixilation due to fiber-cores. Middle: Filtered FCM image. Right: Comparison with confocal microscope (scale bar is 10 μm). (e) Power loss across the FOV at different objective depths.

aberrations. We mark the predicted FOV from Table 1 with a dashed circle. The images were processed by band-stop filtering using a spatial fast Fourier transform (Matlab) to remove the fiber pattern artifact, illustrated in Fig. 2(d). Individual cell bodies and neuronal processes can be resolved in the image, showing sub-cellular resolution, comparable to the standard confocal microscope images obtained with a 10× 0.3 NA objective lens. The effects of distortion and NA variations are not visible within the predicted FOV. We experimentally measured the power loss across the FOV using a thick fluorescence test slide (Chroma Corp.) shown in Fig. 2(e). The decreasing signal is due to the effects of vignetting and aberrations toward the edge of the FOV and was unchanged when varying the axial focus. In conclusion, increasing the objective position only reduces the FOV while otherwise maintaining similar image quality.

We experimentally verified the axial scan range of our FCM. We used a nanopositioner stage (Mad City Labs, LP100) with 100-μm Z-scan range as an axial ruler. We imaged a thick test sample consisting of 1-μm-diameter red fluorescent beads (Invitrogen, F8887), embedded in agarose gel, using 561-nm excitation light. Initially, we fixed the EL at the shortest focal length and obtained axial image sections at 1-μm intervals using the scanning Z-stage. Next, we fixed the sample position and obtained 36 optical sections of the same regions by varying the EL across the full focal range. Figure 3(a) shows an orthogonal projection of several beads resulting from varying the stage position and the EL focal length. Figure 3(b) shows the mapping of bead axial centroids from the stage position to the EL focal setting. Data collected from 40 beads agree with the simulated focal length dependence obtained in the Zemax model. We conclude that our FCM provides a scan range of approximately 80 μm.

We tested the lateral and axial resolution by imaging agarose samples containing 2-μm or 1-μm red fluorescent beads. We set the confocal pinhole on the microscope either to the open position, allowing light collection from multiple fibers, or closed down to a setting of 2 Airy patterns, which allows light collection from only one fiber.

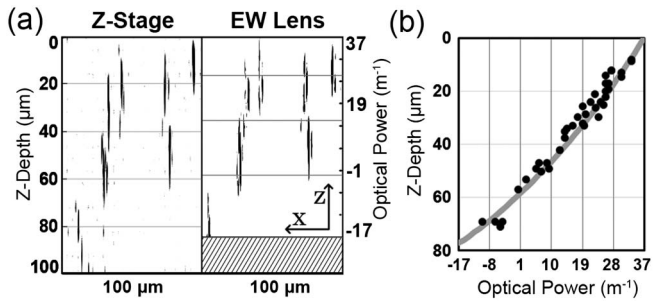


Fig. 3. Axial scan range of electrowetting FCM. (a) Orthogonal projection (inverted grayscale) of 1-μm-diameter red fluorescent beads in agarose imaged with scanning Z-stage (left) and scanning the EL (right). Horizontal gray lines indicate Z-depths of 20, 40, 60, and 80 μm from shortest focus. (b) Black dots: 40 beads mapped from EL optical power to relative Z-position. Gray line: Simulated FCM focal length with varying EL power.

Figure 4(a) shows lateral and axial bead images. With the pinhole open, out-of-focus fluorescence leaks into adjacent fibers, but is eliminated by closure of the pinhole due to the confocal sectioning provided by the fiber cores. Figures 4(b) and 4(c) are imaged with the closed pinhole. The theoretical resolution limit is shown (gray line) using the equations for the full width at half-maximum (FWHM) for lateral resolution in Eq. (1) and the pinhole-limited axial resolution in Eq. (2) [28]:

$$\mathrm{FWHM}_{\mathrm{Lateral}} = 0.51\frac{\lambda}{\mathrm{NA}}, \tag{1}$$

$$\mathrm{FWHM}_{\mathrm{Axial}} = \sqrt{\left(\frac{0.88\lambda}{(n-\sqrt{n^2-\mathrm{NA}^2})}\right)^2 + \left(\frac{n\sqrt{2}\,\mathrm{PH}}{\mathrm{NA}}\right)^2}. \tag{2}$$

The calculations use object-space NA = 0.35, refractive index of air, wavelength $\lambda = 600$ nm, and pinhole diameter PH = 1 μm (2.5 μm fiber-core size demagnified by 2.5×). As shown in Fig. 4(b), the 1-μm-diameter beads occupy a single fiber core, while the 2-μm beads are sampled by multiple cores. This indicates that our FCM

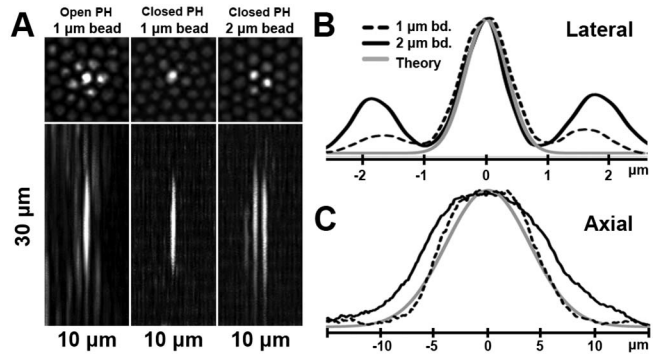


Fig. 4. Lateral and axial resolution of FCM. (a) Lateral and axial images of fluorescent beads. Left: 1-μm bead with open pinhole (PH), Middle: 1-μm bead with closed PH, Right: 2-μm bead with closed PH (b) Averaged line profiles of several 1- and 2-μm beads (black lines) compared with diffraction-limited resolution (gray line) (c) Averaged axial profile of several 1- and 2-μm beads (black lines) compared with theoretical axial resolution (gray line).

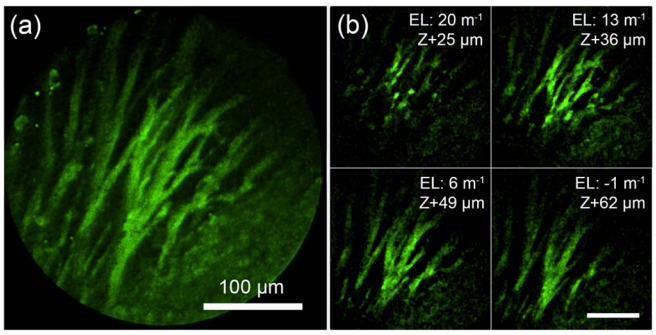


Fig. 5. 3D imaging of mouse nerve tissue. (a) Maximum intensity projection of an image stack of intact olfactory neuron axons labeled with YFP. (b) Four optical sections that were taken at specific EL optical power settings. (Scale bar is 100 μm). See Media 1 for 3D reconstruction.

lateral resolution is fundamentally limited by the fiber core spacing. We estimate the lateral resolution to be 1.8 μm, determined by demagnifying the 4.5-μm core spacing by 2.5×, compared to the theoretical 0.87-μm resolution from Eq. (1). As shown in Fig. 4(c), the FWHM axial resolution is determined to be ∼10 and ∼12 μm for the 1- and 2-μm-diameter beads respectively, compared to the theoretical 9.3-μm resolution.

To demonstrate imaging in tissue with our FCM, we imaged intact mouse olfactory nerve fibers expressing yellow-fluorescent protein in olfactory neurons [29]. The mouse was sacrificed by $CO_2$ inhalation and the head was bisected sagittally to expose the olfactory epithelium and nerve. The FCM was held in position adjacent to the tissue using a manipulator arm with an aqueous saline solution interface between the objective lens and tissue. Imaging was performed using a 488-nm CW laser at a resolution of 1024 × 1024 pixels at 1.7 s/frame. Thirty six image slices were taken while varying EL optical power from 13 to −5 $m^{-1}$. The images were post-processed by band-stop filtering [as seen in Fig. 2(d)]. Figure 5(a) shows a maximum-intensity projection of a stack of optical sections. The diameter of each axonal bundle is ∼10 μm and is easily resolved with our system. Figure 5(b) shows four separate optical sections spanning ∼50 μm, limited by light scattering in the tissue. Each image represents a ∼12 μm optical section with distinct morphological features, demonstrating efficient optical sectioning with our device.

We have demonstrated for the first time that electrowetting variable focus lens technology can be used in a FCM to allow 3D fluorescent tissue imaging. We show a FOV of ∼300 μm, and ∼1.8 μm lateral and ∼12 μm axial resolution. We verified experimentally an axial scan range of 80 μm. We have obtained 3D images of detailed nerve fibers showing axonal networks. We show a lightweight adapter that can be used as a head-mounted device for brain imaging. This design has potential for multiphoton imaging using dispersion compensation. Further improvement of low-voltage EL technology will allow for more diverse endoscopic applications [25]. This approach is promising for use as an implantable brain device because it has no mechanical fatigue, no vibration, and low power usage.

The authors acknowledge financial support from NSF IDBR grant DBI-1353757, NIH DC00566, NIH DC004657, NIH HD041697, and the Butcher Foundation.

**References**

1. F. Helmchen and W. Denk, Nat. Methods **2**, 932 (2005).
2. D. Dombeck, A. Khabbaz, and F. Collman, Neuron **56**, 43 (2007).
3. W. Göbel, B. M. Kampa, and F. Helmchen, Nat. Methods **4**, 73 (2007).
4. A. Pérez-Alvarez, A. Araque, and E. D. Martín, Front. Cell. Neurosci. **7**, 51 (2013).
5. B. A. Flusberg, E. D. Cocker, W. Piyawattanametha, J. C. Jung, E. L. M. Cheung, and M. J. Schnitzer, Nat. Methods **2**, 941 (2005).
6. J. N. D. Kerr and A. Nimmerjahn, Curr. Opin. Neurobiol. **22**, 45 (2012).
7. F. Helmchen, W. Denk, and J. N. D. Kerr, Cold Spring Harb. Protoc. **2013**, 904 (2013).
8. J. Knittel, L. Schnieder, G. Buess, B. Messerschmidt, and T. Possner, Opt. Commun. **188**, 267 (2001).
9. W. Göbel, J. N. D. Kerr, A. Nimmerjahn, and F. Helmchen, Opt. Lett. **29**, 2521 (2004).
10. M. Osanai, T. Suzuki, A. Tamura, T. Yonemura, I. Mori, Y. Yanagawa, H. Yawo, and H. Mushiake, Neurosci. Res. **75**, 46 (2013).
11. R. P. J. Barretto and M. J. Schnitzer, Cold Spring Harb. Protoc. **2012**, 1029 (2012).
12. H. Ra, W. Piyawattanametha, M. J. Mandella, J. T. C. Liu, L. K. Wong, T. D. Wang, C. H. Contag, G. S. Kino, and O. Solgaard, Opt. Express **16**, 7224 (2008).
13. S.-C. Chen, H. Choi, P. T. C. So, and M. L. Culpepper, J. Microelectromechanical Syst. **23**, 570 (2014).
14. L. Liu and H. Xie, IEEE Photon. Technol. Lett. **25**, 1478 (2013).
15. Z. Qiu and W. Piyawattanametha, Displays **36**, 41 (2015).
16. T. Meinert, N. Weber, H. Zappe, and A. Seifert, Opt. Express **22**, 31529 (2014).
17. D. Rivera and C. Brown, Proc. Natl. Acad. Sci. **108**, 17598 (2011).
18. D. G. Ouzounov, D. R. Rivera, W. W. Webb, J. Bentley, and C. Xu, Opt. Lett. **38**, 3103 (2013).
19. N. Koukourakis, M. Finkeldey, M. Stürmer, C. Leithold, N. C. Gerhardt, M. R. Hofmann, U. Wallrabe, J. W. Czarske, and A. Fischer, Opt. Express **22**, 6025 (2014).
20. J. M. Jabbour, B. H. Malik, C. Olsovsky, R. Cuenca, S. Cheng, J. A. Jo, Y.-S. L. Cheng, J. M. Wright, and K. C. Maitland, Biomed. Opt. Express **5**, 645 (2014).
21. F. O. Fahrbach, F. F. Voigt, B. Schmid, F. Helmchen, and J. Huisken, Opt. Express **21**, 21010 (2013).
22. L. Chen, S. Kumar, D. Kelly, N. Andrews, M. J. Dallman, P. M. W. French, and J. Mcginty, Biomed. Opt. Express **5**, 3367 (2014).
23. B. Berge and J. Peseux, Eur. Phys. J. E **3**, 159 (2000).
24. M. Blum, M. Büeler, C. Grätzel, and M. Aschwanden, Proc. SPIE **8167**, 81670W (2011).
25. R. D. Niederriter, A. M. Watson, R. N. Zahreddine, C. J. Cogswell, R. H. Cormack, V. M. Bright, and J. T. Gopinath, Appl. Opt. **52**, 3172 (2013).
26. W. Piyawattanametha, E. D. Cocker, L. D. Burns, R. P. J. Barretto, J. C. Jung, H. Ra, O. Solgaard, and M. J. Schnitzer, Opt. Express **34**, 2309 (2010).
27. M. Born and E. Wolf, *Principles of Optics*, 6th ed. (Cambridge University, 1999).
28. J. Pawley, *Handbook of Biological Confocal Microscopy*, 3rd ed. (Springer, 2006).
29. A. Li, D. H. Gire, T. Bozza, and D. Restrepo, J. Neurosci. **34**, 16058 (2014).